Journal of Materials Chemistry A

PAPER

View Article Online
View Journal | View Issue

Cite this: J. Mater. Chem. A, 2017, 5, 3900

Micro-solid state energy conversion membranes: influence of doping and strain on oxygen ion transport and near order for electrolytes†

Yanuo Shi,[a] Iñigo Garbayo,[a] Paul Muralt[b] and Jennifer Lilia Marguerite Rupp*[a]

Received 18th October 2016
Accepted 8th January 2017

DOI: 10.1039/c6ta09035d

www.rsc.org/MaterialsA

Enhancing the efficiency of micro-energy conversion devices through engineering of the structure–transport relationship is a prerequisite toward next generation micro-electrolysers and fuel cells. Here, oxygen ion conducting free-standing thin films are key elements, forming buckled and strained membranes for gas exchange and energy conversion. The electro-chemo-mechanics of free-standing membranes *vs.* substrate-supported films are investigated as model device structures to study the factors influencing the ionic transport, and answer the fundamental question: how strongly does solid solution doping *vs.* lattice strain affect the defect-induced oxygen ion transport in buckled electrolyte membrane films for solid state micro-devices? Importantly, we demonstrate that tuning the electro-chemo-mechanics of doped ceria films can influence the ionic transport through the effect of opposed strained volumes altering the clustering of oxygen vacancy defects. Strain is studied by comparing flat substrate-supported films to compressive buckled membrane devices and observing subsequent changes in atomistic near order *via* Raman spectroscopy. The buckling resulted in a significant increase of the activation energy for ionic transport, greater than classical extrinsic doping. The power of electro-chemo-mechanic engineering of ceramic films is demonstrated in finding the best strategy for optimizing ionic conduction and thereby enhancing future performance in thin film electrolytes for micro-energy conversion devices.

Introduction

The study, control and modification of functional thin films is playing a core role on the optimization of "ionotronic devices" for future energy and information harvesting such as miniaturized solid oxide fuel cells,[1–4] solid-state batteries[5–8] or resistive random access memories.[9–12] Classical strategies for tuning of oxygen ion transport kinetics have focused on the structural lattice modification of the oxide material through solid solution doping which can influence both association and migration energies.[13] However, recent studies have also shown the relevance of mechanical strain state changes as a new source for modifying the electrochemical properties such as oxygen ion transport and ion exchange for thin films.[14–25] This involves improving oxygen ion mobility by generating defects such as oxygen vacancies in heterostructures of electrolyte films,[14–17,26,27] suppressing phase changes to keep a fast oxygen conducting phase,[28] minimizing edge dislocations[29] or minimizing defect associations.[30–33] There is an increasing interest in studying "electro-chemo-mechanic" coupling, *i.e.* the correlation between ionic transport, chemical stoichiometry and mechanical lattice strain, for the optimization of functional oxide film materials.[3,34,35]

In the field of micro-energy conversion devices, doped ceria and zirconia thin films are the state-of-the-art electrolyte materials and have been intensively investigated.[36–47] Classic micro-solid state energy conversion device designs are mostly based on the fabrication of functional free-standing membranes for the electrolyte and electrode assemblies to ensure gas access from both sides and, hence, chemical-to-electrical energy conversion of the cells; *i.e.* micro-solid oxide fuel cells or electrolysers.[2,36,48] In such a thin film membrane-based device one cornerstone for its optimization is the fabrication of a gas tight, highly conductive and thermo-mechanically stable free-standing electrolyte film.[49,50] Additionally, improvement of electrode film performance is also critical. For doped ceria and zirconia thin film electrolytes, it has been shown that the mechanical properties of such free-standing electrolyte membranes depend on multiple external

[a]Electrochemical Materials, Department of Materials, ETH Zürich, Switzerland. E-mail: jennifer.rupp@mat.ethz.ch

[b]Ceramics Laboratory, Ecole Polytechnique Fédérale de Lausanne EPFL, Lausanne, Switzerland

† Electronic supplementary information (ESI) available: More details on the fabrication process of free-standing electrolyte membranes with microelectrodes, the comparison between free-standing and substrate-supported gadolinia-doped ceria thin films, the full width at half maximum (FWHM) of F_{2g} mode as a function of compressive net strain, and the details of the impedance spectroscopy measurement are provided in supporting materials. See DOI: 10.1039/c6ta09035d

parameters, such as the membrane aspect ratio,[51] buckling geometry[52] and the initial choice of film fabrication parameters, *e.g.* atomic peening effects in physical vapor deposited films.[3,42] From a device perspective, optimization of the conversion power is still a major issue for micro-energy conversion membranes. By analyzing current power data published for micro-solid oxide fuel cells, it can be concluded that even if the same materials and cell designs are used the power output currently varies from 26 to 1037 mW cm^{-2} when comparable open circuit voltages were obtained at 500 °C.[2,36] This is a major issue and requires attention: one hypothesis is that unlike classic large-scale ceramic cells, strain effects strongly influence the transport properties of thin film components in these devices. The effective compressive in-plane strain state may modify the oxygen migration and association energies in doped electrolyte films processed as buckled membranes. Importantly, it has to be noted that often the strain states are not measured or mentioned in the reports with respect to the electrolyte membrane characteristics after processing for micro-energy conversion devices. Being under high mechanical stress, the manipulation of oxygen ion transport in the electrolyte may be greatly affected by local strain fields in addition to the extrinsic doping level. Such an effect would be comparable to current investigations in heterolayers where strain fields are generated intentionally through interface modulations in oxygen ion conductors, *e.g.* ref. 15 and 53. For example, more than 3 orders of magnitude increased conductivity was observed on tensile-strained yttria-stabilized zirconia films compared to films under compression, see reviews.[16,17,54] Despite the progress, investigations miss looking at the fundamental question of how variations in doping concentration (*i.e.* x in $Gd_xCe_{1-x}O_{2-\delta}$) and atomistic strain affect changes in the strength of oxygen anionic–cationic bonds, measured *via* Raman vibrational spectroscopy of free standing buckled electrolyte film membranes (relative to flat substrate-supported structures[55]). The implication of these properties on the oxygen ion transport is to be measured with respect to both the *doping concentration* and *strain*, and may present new insights into future design and enhanced performance of micro-energy conversion devices.

Design of the experiment

Through this study, we suggest a model experiment to fundamentally probe the implications of changes in the *doping concentration* and *lattice strain* on the near order ionic structures and the ionic conduction for electrolyte thin film membranes. It is very well known that the difference in ionic radii between an extrinsic dopant and host atom can be used to generate sites for vacancies and ions to migrate. In general, the presence of any doping atom has an effect on the lattice constant and thus induces lattice strain, which becomes particularly significant when working with thin films, as shown for zirconia and ceria-doped materials.[30,56–59] However, the implication of the doping concentration changes on the local near order bond strength changes, local buckling patterns of membrane films, and local strain states are still to be investigated with respect to the ionic transport for these electrolytes. Here we design a model experiment in which, on the one hand, the trivalent gadolinia dopant concentration in ceria is systematically varied to modify the defect association energy, and also the in-plane compressive strain state is analyzed for two film structures, flat *substrate-supported films* and buckled *free-standing membranes* (*i.e.* a real device structure). The influence of doping and strain is studied by observing changes in the oxygen ion transport and nanoscopically on the near order for the oxygen anionic–cationic bonds by AC impedance spectroscopy and Raman spectroscopy, respectively. To the best of our knowledge, we are not aware of studies looking at effects of changes in the doping concentration on oxygen ion transport and ionic near order changes for real membrane device structures. These results contribute to the fundamental understanding of how the doping and/or strain variation influence the oxygen ion transport of functional thin films. Importantly, the changes in the electro-chemo-mechanics are studied for real buckled micro-energy solid-state conversion devices integrated on a silicon chip-based device.

Thin ceria-based films with three different doping concentrations were fabricated: namely, undoped ceria, 10 mol% and 20 mol% gadolinia-doped ceria. For this, 270 ± 20 nm thick films were deposited by pulsed laser deposition (PLD) at 400 °C, over 200 nm thick Si_3N_4 on Si substrates. Square shaped free-standing membranes were released by etching the Si substrate from the rear side and removing the Si_3N_4 layer underneath the ceria-based film by reactive ion itching (RIE) (see Fig. S1 of the ESI† for further details on the fabrication process). Samples with and without the etching step were processed and analyzed to directly compare the strain and ionic transport properties of *free-standing membranes* and *substrate-supported films*.

Results and discussion

Fig. 1a demonstrates an exemplarily array of 36 free-standing and pristine CeO_{2-x} membranes fabricated on a Si_3N_4/Si substrate. We display in Fig. 1b an optical micrograph of a 350 μm × 350 μm wide and free-standing ceria thin film membrane. In this image, the microelectrode design used in this work can be observed. For both substrate-supported and free-standing samples, 100 nm thick Pt microelectrodes were patterned by e-beam evaporation using a shadow mask during the deposition. This results in four symmetric Pt microelectrode pins separated by a minimum distance of ~150 μm and a diagonal distance of ~210 μm. Fig. 1c shows a cross-sectional image of a free-standing undoped ceria membrane, as obtained by focused ion beam cutting and secondary electron imaging in a scanning electron microscope. A dense CeO_2 film is visible as a free-standing membrane and one of its top Pt electrode with good adherence to the oxide.

The buckled free-standing membrane and the flat substrate-supported film sample geometries are illustrated schematically in Fig. 1d. By processing the same microelectrode patterns on the buckled membranes and flat substrate-supported films, we can compare two different strain states acting on the thin film lattices. In addition to changes in the doping concentration, this systematic variation of strain states makes these devices a model case for studying relationships between the near order

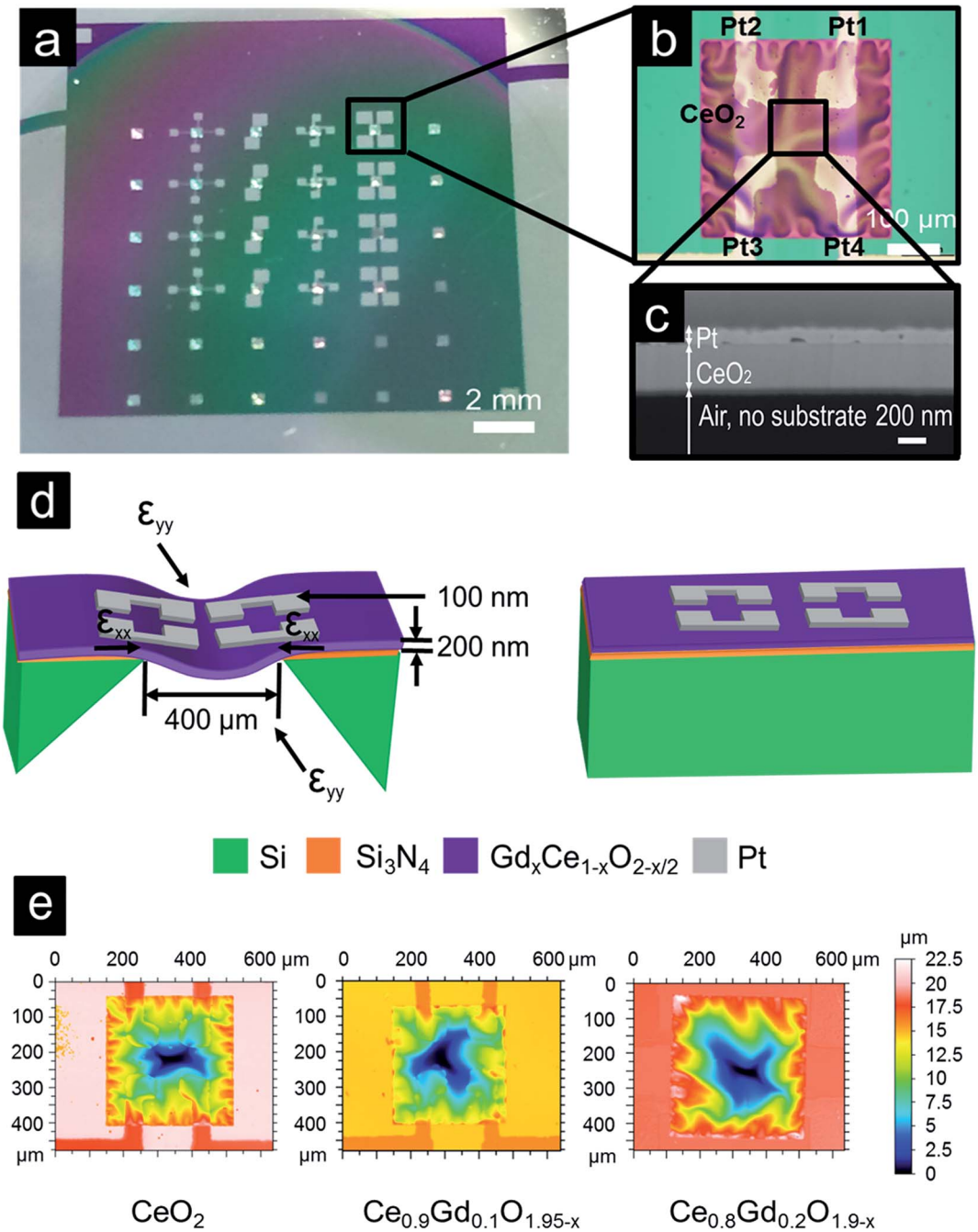

Fig. 1 (a) Optical image of 36 micro-energy conversion membranes with 6 × 6 array of free-standing buckled ceria membranes. (b) Optical microscopy image of one single membrane, where the Pt microelectrodes can be identified. (c) Cross-sectional view of a free-standing ceria membrane with the top electrode, accessed through focused ion beam cutting and scanning electron microscopy. (d) Schematic for free-standing and substrate-supported thin film devices, with an integrated micro-top electrode suited for measurements of ionic transport and determination of relative net strains in-between the electrodes. (e) Buckling patterns of the undoped and doped free-standing membranes measured by optical profilometry.

changes in vibrational bonds, thin film buckling and ionic transport. First, the buckling profile of the free-standing membranes was studied as a function of its gadolinia doping concentration by optical microscopy and subsequent buckling analysis. Fig. 1e shows the buckling pattern of three representative free-standing membranes measured by optical profilometry, corresponding to the three different doping levels studied. In all cases, highly buckled membranes were obtained after free-etching. However, the local buckling distribution over the area of each ceria-based membrane varies respectively with its doping concentration. While the buckling deformation of the pristine CeO_2 membrane appears rather symmetric and membrane-centered, for membranes with 10 mol% of gadolinia doping or more the maximum buckling position along the

diagonal direction formed more asymmetric patterns. Moreover, the maximum out-of-plane deformation between the same electrode pins on free-standing CeO_2, $Ce_{0.9}Gd_{0.1}O_{1.95-x}$ and $Ce_{0.8}Gd_{0.2}O_{1.9-x}$ is 9.0 ± 0.09 μm, 11.5 ± 0.2 μm and 14.6 ± 0.3 μm, respectively. The growing asymmetry of the buckling patterns with respect to the doping concentration suggests that the Poisson's ratio may not be a constant anymore in this state and confirms that inelasticity has to be taken into account when increasing the doping concentration of the films, *i.e.* the elastic tensor is no longer symmetric for the cubic structures of the ceria-based ionic conductor. Our finding agrees well with earlier reports by Lubomirsky and co-workers,[60] on single membrane films without top-electrode designs. Note that this observation highlights a potential change of inelasticity and Poisson's ratio with changing dopant amount in the thin film under strain.

Using the von Karman plate model,[51,52,61] the strain in the buckled ceria-based films was quantified by analyzing the buckling pattern of the membranes and the maximum out-of-plane deformation between the microelectrodes, see ref. 3 for details. Substrate-supported samples are assumed to have zero net compressive strain (no deformation), and are taken as base reference for the buckled film.[3] In-plane net compressive strains of 0.68 ± 0.02%, 1.11 ± 0.04% and 1.78 ± 0.07% were measured in the buckled membranes for the undoped, 10 mol%, and 20 mol% membranes, respectively. These compressive strains of membranes result mainly from (i) the thermal expansion mismatch of the thin film and substrate (films were deposited by PLD at 400 °C), (ii) a compressive stress coming from the atomic peening effect during film growth, typical of all vapor deposition processes (see ref. 39 and 62–65 for detailed discussion), and, importantly, (iii) the effect of solid solution doping and changed elastic constants.

We now examine the near order oxygen anionic–cationic vibrational changes of the strained free-standing membranes and flat substrate-supported films by micro-Raman spectroscopy, Fig. 2. This offers the possibility of studying doping and strain effects on the lattices and ionic bonding environments. Fig. 2a illustrates the measuring configuration, and how atomistic near order characteristics of membranes' local strain state is characterized using Raman. For buckled ceria membranes, the incident laser beam is focused to a point where the incident beam is perpendicular to the bended surface under in-plane compressive strain. For measuring the flat substrate-supported films, the incident beam is also set perpendicular to the surface. The cubic fluorite lattice structure of ceria and its doped species reveal only one single allowed Raman vibration mode, namely the F_{2g} stretching vibration, which is highlighted in the lattice schematic in Fig. 2a. The F_{2g} Raman stretching vibrational mode represents the local oxygen anionic–cationic bonding of the thin films and is analyzed as a function of the doping level and film strain state (substrate-supported and flat, or free-standing and buckled). The Raman spectra of flat substrate-supported and free-standing buckled ceria-based thin films are compared in Fig. 2b, with respect to the gadolinia doping concentration, as well as the spectrum of the Si–Si_3N_4 substrate measured with an excitation laser wavelength of 633 nm and 300 g mm^{-1} grating. The F_{2g} mode peak is visible in all spectra from the thin films, appearing always in the range between 463 and 466 cm^{-1}, which is in general agreement with the literature on ceria-based bulk macro-pellets and substrate-supported films.[30,66,67] Additionally, in the case of the flat substrate-supported films, the peaks of the Si substrate are also noted in the spectra.[68] Finally, on the free-standing membranes the second phonon scattering peak α at ∼250 cm^{-1} was slightly detectable for $Ce_{0.8}Gd_{0.2}O_{1.9-x}$, while in the lower doped samples phonon scatter peaks remained invisible.

First, we turn to the flat substrate-supported films to analyze the changes in vibration of the F_{2g} mode with respect to the solid solution doping. Increasing the concentration of the gadolinia doping up to 20 mol% results in the F_{2g} wavenumbers changing from 464.9 ± 0.07 cm^{-1} to 463.8 ± 0.11 cm^{-1} and then rising to 464.7 ± 0.17 cm^{-1}, Fig. 2c. A similar trend was observed for the case of free-standing membranes, but at generally increased wavenumbers: the F_{2g} peak moved from 465.1 ± 0.06 cm^{-1} to 464.2 ± 0.01 cm^{-1} then to 465.8 ± 0.11 cm^{-1}, Fig. 2c. The changes in Raman frequency shift observed here are in agreement with doping concentration changes in the solid solution series similar to bulk ceria pellets with trivalent rare earth dopants.[67,69,70]

Interestingly, the F_{2g} peak measured on CeO_2, $Ce_{0.9}Gd_{0.1}O_{1.95-x}$ and $Ce_{0.8}Gd_{0.2}O_{1.9-x}$ free-standing membranes presented shifts generally towards higher wavenumbers of +Δ0.2 ± 0.09 cm^{-1}, +Δ0.4 ± 0.11 cm^{-1} and +Δ1.1 ± 0.20 cm^{-1} when compared with the flat substrate-supported samples, Fig. 2c. Also, we clearly observe that the changes in the Raman shift when turning a flat in-plane strained film to a buckled membrane are larger for increased doping concentrations of gadolinia in ceria; *viz.* when increasing the oxygen vacancy concentration. Combined with the local strain obtained through the analysis of membrane buckling by optical profilometry, the relationship between the F_{2g} peak shifts and strain changes when releasing membranes was plotted as shown in Fig. 2d. Shifts towards higher wavenumbers in Raman, *i.e.* positive ΔF_{2g} in Fig. 2d, are typically associated with higher in-plane compressive strain.[3,15,71] Additionally, we observe an F_{2g} peak broadening with increasing doping concentration, and also when turning the originally flat to the buckled membranes and lattices, see the analysis of full width at half maximum (FWHM) in Fig. S2 of the ESI.† This observation is in agreement with the earlier Raman literature of Aldinger and co-workers, who noted broadening of the F_{2g} peak in doped ceria materials with decreasing thin film crystallinity and increasing structural disturbances.[72] In our case, the observed peak broadening might reflect a higher defect density with increased doping, as well as microstructural changes resulting from compressive strain resulting from releasing the membranes.

In summary, substantial shifting towards high wavenumbers in the oxygen anionic–cationic F_{2g} bond vibration peak position and peak broadening (quantified *via* FWHM) were detected when the thin films were turned to free-standing buckled membranes. *E.g.* the F_{2g} peak is increased to 465.8 ± 0.11 cm^{-1} for net compressive strains up to 1.78 ± 0.07% for $Ce_{0.8}Gd_{0.2}O_{1.9-x}$ free-standing membrane. Spectral changes observed when comparing substrate-supported and buckled membranes

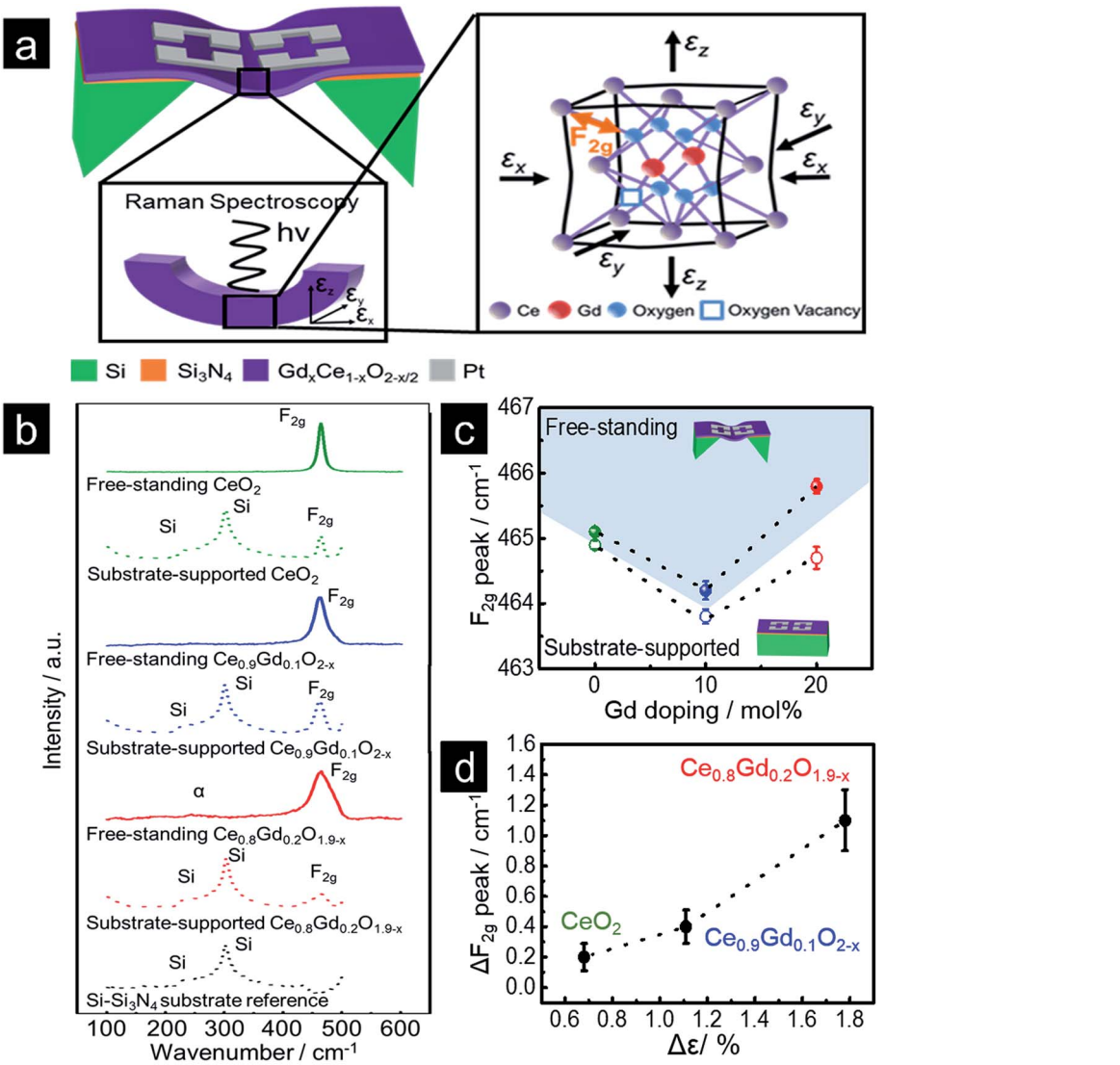

Fig. 2 Atomistic near order characteristics of substrate-supported and free-standing gadolinia-doped ceria thin films through micro-Raman spectroscopy with respect to solid solution doping. (a) Schematic view illustrating the near order bonding and probing directions *via* Raman spectroscopy. The Raman active F_{2g} bond is highlighted as well as strain tensor directions. (b) Raman spectra of flat substrate-supported and buckled free-standing ceria-based films with respect to the doping concentration. The cationic–oxygen anionic Raman F_{2g} single modes, as well as α 2nd order phonon scattering on the free-standing $Ce_{0.8}Gd_{0.2}O_{1.9-x}$ membrane, are indicated. (c) Comparison of the Raman F_{2g} cationic–oxygen anionic stretching mode peak center of ceria-based films as a function of the Gd doping concentration. (d) Measured shifts on the Raman F_{2g} peak comparing flat substrate-supported and buckled free-standing films as a function of the net compressive strain change measured by optical profilometry.

could relate to the presence of the tensile Si_3N_4 layer present on top of the Si substrate,[3] which would reduce the overall compressive strain in the substrate-supported films, but would have negligible influence on the free-standing membranes. Additionally, doping also affects ΔF_{2g} and the broadening of the peaks. In general, this might reflect changes in the order of oxygen vacancies in the sub-lattices under different strain levels, which would be more significant with increased doping. This conclusion might be supported by the observation of additional phonon scatter modes α appearing in the $Ce_{0.8}Gd_{0.2}O_{1.9-x}$ free-standing membranes.[3] However, to the best of our knowledge we cannot compare these novel Raman insights on the role of the 2nd order phonon scattering on oxygen vacancies to other literature on ceria-based materials under mechanical stress, but report that we only observe this effect in the spectra of the $Ce_{0.8}Gd_{0.2}O_{1.9-x}$ free-standing membrane.

Motivated by these results we turn now to the effect of doping and compressive lattice strain on oxygen ion transport of buckled and flat doped ceria thin films. The ionic conductivity for the different ceria-based films with different doping concentrations was measured in-plane between the two opposite microelectrodes Pt2 and Pt4, see Fig. 1b. Electrolyte ionic resistivity was obtained through electrochemical impedance spectroscopy,[73] detailed in ESI S3.† Fig. 3a represents an Arrhenius plot of the ionic conductivity for the free-standing and substrate-supported doped ceria films with respect to

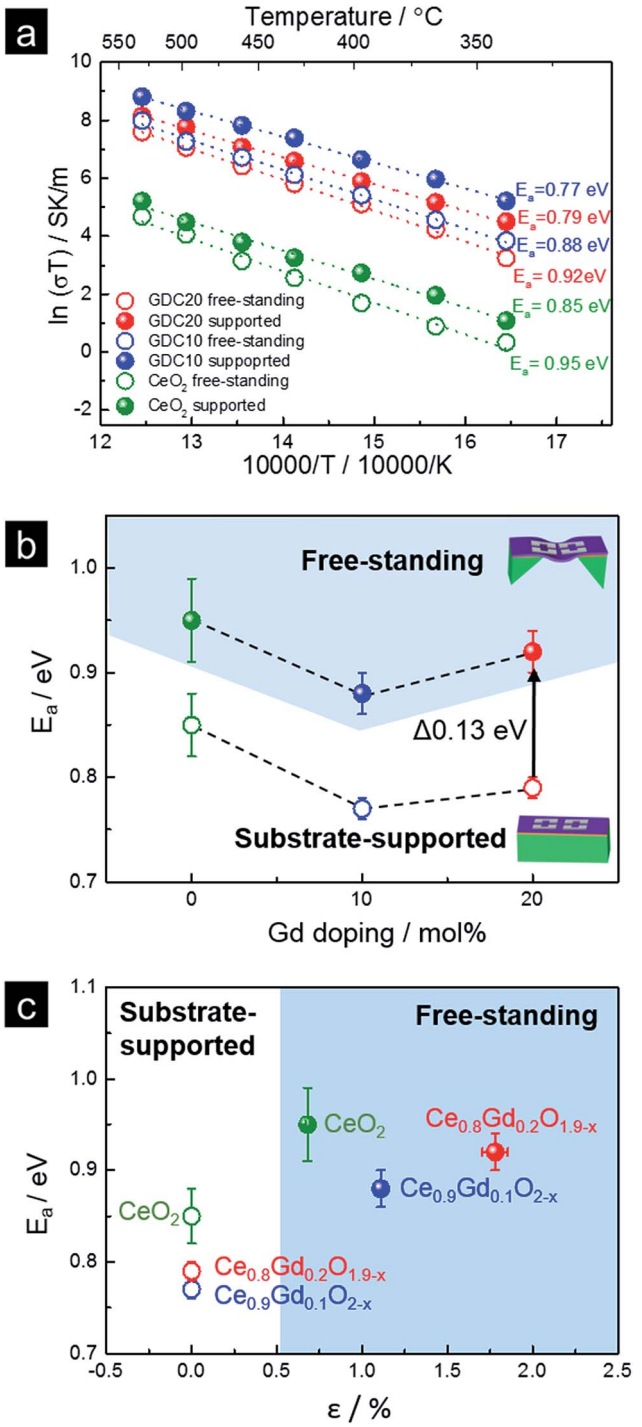

Fig. 3 Strain–ionic transport interactions on substrate-supported films and free-standing membranes of CeO_2, $Ce_{0.9}Gd_{0.1}O_{1.95-x}$ (GDC10) and $Ce_{0.8}Gd_{0.2}O_{1.9-x}$ (GDC20). (a) Arrhenius type diagrams of the in-plane total ionic conductivity for the substrate-supported films and free-standing membranes with respect to the doping concentration. (b) Activation energy of total ionic conductivity as a function of the doping concentration for the flat substrate-supported and buckled free-standing membranes. (c) Activation energy of ionic conductivity *vs.* net compressive in-plane strain for flat reference substrate-supported films and buckled free-standing membranes, with respect to the doping concentration.

dopant concentrations ranging from 0 to 20 mol%. We first turn to study the effect of doping for the ceria-based thin films and exemplify on the *substrate-supported films*: when the dopant concentration is raised from 0 to 10 mol%, the activation energy (E_a) is reduced from 0.85 ± 0.03 eV to 0.77 ± 0.01 eV. Meanwhile, further increasing of the doping concentration to 20 mol% results in an activation energy of 0.79 ± 0.01 eV, see Fig. 3b. The activation energies measured here for the three different substrate-supported thin films match previous references on spray pyrolysis, flame spray and PLD processed films studied with respect to extrinsic doping of gadolinia.[15,54,74] Similarly, the *free-standing membrane* activation energies present the same evolution, *i.e.* from 0.95 ± 0.04 eV to 0.88 ± 0.02 eV and 0.92 ± 0.02 eV for doping concentrations 0 mol%, 10 mol% and 20 mol% of gadolinia, respectively, with activation energies that were generally greater when compared with substrate-supported films. In summary, we measure an optimum doping concentration at 10 mol% of gadolinia for which in-plane conductivity is the highest; this trend holds within the series of the flat substrate-supported films, as well as for the buckled free-standing membranes, Fig. 3a.

Secondly, we assess whether there is an effect of lattice strain on the ionic transport of the undoped and doped ceria thin films. To exemplify that, the activation energy of ionic transport was plotted in Fig. 3c *versus* the membrane net compressive strain measured by optical profilometry between the electrodes. It can be observed that the activation energy of ionic conduction increased in all doping cases when the originally flat substrate-supported films turn into buckled free-standing membranes: a maximum of +Δ0.13 eV was observed for the $Ce_{0.8}Gd_{0.2}O_{1.9-x}$ free-standing membrane for a +1.78% net compressive strain when compared to the flat substrate-supported film. Slightly smaller changes in activation energies were also measured for the less strained films of $Ce_{0.9}Gd_{0.1}O_{1.95-x}$ and pure ceria: +Δ0.11 eV and +Δ0.10 eV, respectively. These findings reveal that not only does altering the doping amount significantly affect the total ionic conductivity, but also the engineering of lattice strain patterns in these oxygen ion conducting membranes affects the overall transport strongly *via* significant changes in the migration activation energy.

Conclusions

In conclusion, this work analyzed the effect of compressive lattice strain and extrinsic doping on the Raman vibrations and related ionic transport properties of gadolinia-doped ceria micro-energy conversion membrane-based device structures. It has been shown that when changing the net compressive lattice strain up to 1.78%, changes in the local near order F_{2g} oxygen–cationic bonds are observed as the ionic bond strength increases, indicated by measurable Raman peak shifts. Purely analyzing the effect of doping, the wavenumber of F_{2g} mode decreases when moving from undoped ceria to 10 mol% doped, for increasing again to higher wavenumbers with increasing doping (to 20 mol%). However, when releasing the films to free-standing membranes (*i.e.* changing the strain state) higher wavenumbers are observed for all the doping concentrations.

Larger shifts (ΔF_{2g}) are found when increasing the doping concentration, and a maximum of $\Delta 1.1$ cm^{-1} was measured on the 20 mol% ceria film between substrate-supported and free-standing films. Furthermore, lattice strain measurably affects the activation energy of the total ionic conductivity, and cannot be neglected for engineering principles in these ion conducting membranes. We measure an increase of the activation energy when converting the flat substrate-supported films to buckled free-standing and compressively strained membranes (*i.e.* up to $+\Delta 0.13$ eV for 1.78% strain in 20 mol% doped ceria). We explain this based on careful Raman analysis of the vibrational bond changes in terms of F_{2g} cationic–oxygen anionic stretching mode. Such Raman measurements are still unique within the field of oxygen ion transport membranes and their general validity should be further confirmed by studies in other material systems. However, this study indeed highlights an important potential technique to measure changes in the oxygen vacancy sublattice upon strain on micro-device structures with functional ionic conductors. Analysis of the symmetry of buckling patterns for the free-standing membranes was additionally in line with earlier observations by Lubomirsky *et al.*,[60] where an increased asymmetry is measurable for increasing doping concentration and defect ordering under compressive strain. This suggests that the elastic properties of such stressed ceramic membranes may no longer be treated as constant and highlights a potential change of inelasticity and Poisson's ratio with the changing dopant amount in the thin film under strain.

Through this work, net compressive strain changes up to 1.78% demonstrated in the given model case strongly influence the activation energy of ionic transport and ionic near order bond changes, whose impact is comparable to tailoring the doping concentration up to 20 mol% for ceria films. For future engineering and designs of micro-energy conversion and storage devices, strain engineering has a competing role and can actively be used as a tool to maximize the compressive in-plane strains to allow for fast conduction in the out-of-plane, tensilely strained electrolyte directions. In addition, numerous studies have shown a clear change in the oxygen reduction reactions with respect to strain state of single cathode films to tune the losses.[18,19,75–78] Here we contribute to the discussion on showing the importance of engineering not only the electrolyte doping composition, but also its strain state, which represents a promising basis upon which to optimize future Si chip-based energy conversion complex devices for real micropowering systems.

Methods

Sample microfabrication

Two kinds of gadolinia-doped ceria samples were used in this experiment: flat substrate-supported thin films and buckled free-standing membranes. To fabricate the substrates, 200 nm thick low-stress Si_3N_4 layers were deposited on both sides of a (100) silicon wafer (4-inch, 380 μm thick) by low pressure-chemical vapor deposition (LP-CVD, Ceramics Laboratory, EPFL). For the substrate-supported films, the ceria-based thin films were directly deposited by pulsed laser deposition (PLD) in such substrates. Meanwhile, for the case of free-standing samples, the Si_3N_4 coated silicon wafers were patterned on one side by photolithography to define the membrane areas. Then the Si_3N_4 was etched only on that side by reactive ion etching (RIE, Oxford Instruments RIE 80+) and the wafer was immersed on a KOH (20 mass%) solution at 90 °C for 7 h to etch the Si and form free-standing Si_3N_4 membranes on the opposite side. Si_3N_4 membranes were then used as substrates for the deposition of ceria-based thin films by PLD. Finally, the Si_3N_4 layers underneath were removed by a 2nd RIE step from the rear side and the ceria free-standing membranes were released. A more detailed fabrication flow to obtain ceria-based free-standing membranes is described in S1 of the ESI† and ref. 3.

Target preparation and thin film deposition of functional films

270 ± 20 nm thick films of the three different materials were deposited by PLD (Surface Technologies, Germany), using a KrF excimer laser with a wavelength of 248 nm. Laser energy was set at 0.67 J cm^{-2} and targets were ablated at a frequency of 10 Hz. The substrates were heated up to 400 °C during deposition and pressure was kept at 0.03 mbar inside the chamber under a constant flow of O_2. For all PLD thin film depositions, ceramic targets fabricated by the authors were used. To fabricate targets, commercial CeO_2, $Gd_{0.1}Ce_{0.9}O_{1.95-x}$ and $Gd_{0.2}Ce_{0.8}O_{1.9-x}$ powders (Sigma-Aldrich, Switzerland) were first pressed uniaxially (440 bar for 2 min), and then isostatically pressed (22 kbar for 2 min) in order to form dense pellets. The pellets were heated to 1400 °C at 3 °C min^{-1}, sintered for 4 hours, and then cooled with 5 °C min^{-1} to room temperature. The final relative theoretical density of the CeO_2, $Gd_{0.1}Ce_{0.9}O_{1.95-x}$ and $Gd_{0.2}Ce_{0.8}O_{1.9-x}$ PLD targets was 81.3%, 88.8%, and 89.4%, respectively.

Strain, microstructure and structural characterization

An optical profilometer (Sensofar, Schaefer-Tec AG) was used for measuring the surface profile of the buckled membranes and flat films. Micro-Raman spectroscopy was carried out on a WITec Alpha300 (Germany) equipped with a 633 nm wavelength laser for excitation, a 300 g mm^{-1} grating, and lateral resolution of 515 nm. At least 5 Raman measurements on the center of the thin film (different positions) were performed for each sample, and the mean value of Raman peak centers was calculated after fitting etch spectra by the Gaussian function. The elastic scattering peak was used to calibrate results of each spectrum under 300 g mm^{-1} grating. Cross-sections of the free-standing membranes were obtained by focused ion beam milling using a scanning electron microscope (SEM) equipped with a Ga^+ ion beam column (FIB-SEM, Zeiss NVision 40), and were imaged in SEM secondary electron mode (LEO 1530, Germany).

Microelectrode processing and electrical characterization

100 nm thick Pt microelectrodes were deposited over the functional free-standing membranes and/or substrate-supported films by electron beam evaporation using specially

designed shadow masks during deposition (physical vapor deposition, Evaporation Plassys II). For micro-electrical characterization, a custom-made microprobe station was used (Electrochemical Materials Group, ETH Zürich, Switzerland and Everbeing Taiwan). The station was equipped with a hotplate for controlled heating up to 550 °C, *in situ* microscopy and videography, electrically shielded micro-manipulators suitable for electrochemical impedance spectroscopy, thermocouple positioners, and a gas flow control system to regulate the atmosphere of the sample. A Reference 600 (Gamry Instruments, USA) was used to measure resistance *via* AC impedance spectroscopy, and all measurements were performed between the diagonal pins of the microelectrodes design shown in Fig. 1b (labelled as Pt2 and Pt4). Further details can be found in ESI S3.† We add more insights into the fabrication process of the membranes and reproducibility in ESI S4.†

Conflict of interest

The authors declare no competing financial interests.

Acknowledgements

Sebastian Schweiger, Electrochemical Materials ETH Zürich, is thanked for the experimental support and discussion of the Raman spectroscopy data. Prof. Ralph Spolenak from the Laboratory for Nanometallurgy, ETH Zürich, is thanked for providing the Raman spectrometer. Prof. Nicholas Spencer and Clément Cremmel, of the Surface Science and Technology group, ETH Zürich, are acknowledged for their assistance with analytical tools of optical profilometry. We also thank the staff of FIRST Center for Micro- and Nanoscience, ETH Zürich, for providing and maintaining the cleanroom facilities used for the microfabrication described herein. Finally, this work was supported by the Swiss National Science Foundation (SNSF) under the project numbers 144988, 147190, and 138914, and SNSF Starting Grant (ERC), project number BSSGIO_155986/1.

References

1 A. Evans, M. Prestat, R. Tölke, M. V. F. Schlupp, L. J. Gauckler, Y. Safa, T. Hocker, J. Courbat, D. Briand, N. F. de Rooij and D. Courty, *Fuel Cells*, 2012, **12**, 614–623.
2 I. Garbayo, D. Pla, A. Morata, L. Fonseca, N. Sabaté and A. Tarancón, *Energy Environ. Sci.*, 2014, **7**, 3617–3629.
3 Y. Shi, A. H. Bork, S. Schweiger and J. L. M. Rupp, *Nat. Mater.*, 2015, **14**, 721–728.
4 D. Pla, A. Sanchez-Gonzalez, I. Garbayo, M. Salleras, A. Morata and A. Tarancon, *J. Power Sources*, 2015, **293**, 264–273.
5 J. F. M. Oudenhoven, L. Baggetto and P. H. L. Notten, *Adv. Energy Mater.*, 2011, **1**, 10–33.
6 S. Afyon, F. Krumeich and J. L. M. Rupp, *J. Mater. Chem. A*, 2015, **3**, 18636–18648.
7 J. van den Broek, S. Afyon and J. L. M. Rupp, *Adv. Energy Mater.*, 2016, **6**, 1600736.
8 M. Rawlence, I. Garbayo, S. Bücheler and J. L. M. Rupp, *Nanoscale*, 2016, **8**, 14746–14753.
9 R. Waser, R. Dittmann, G. Staikov and K. Szot, *Adv. Mater.*, 2009, **21**, 2632–2663.
10 F. Messerschmitt, M. Kubicek, S. Schweiger and J. L. M. Rupp, *Adv. Funct. Mater.*, 2014, **24**, 7448–7460.
11 F. Messerschmitt, M. Kubicek and J. L. M. Rupp, *Adv. Funct. Mater.*, 2015, **25**, 5117–5125.
12 M. Kubicek, R. Schmitt, F. Messerschmitt and J. L. M. Rupp, *ACS Nano*, 2015, **9**, 10737–10748.
13 M. Nakayama and M. Martin, *Phys. Chem. Chem. Phys.*, 2009, **11**, 3010.
14 N. Schichtel, C. Korte, D. Hesse, N. Zakharov, B. Butz, D. Gerthsen and J. Janek, *Phys. Chem. Chem. Phys.*, 2010, **12**, 14596–14608.
15 S. Schweiger, M. Kubicek, F. Messerschmitt, C. Murer and J. L. M. Rupp, *ACS Nano*, 2014, **8**, 5032–5048.
16 B. Yildiz, *MRS Bull.*, 2014, **39**, 147–156.
17 C. Korte, J. Keppner, A. Peters, N. Schichtel, H. Aydin and J. Janek, *Phys. Chem. Chem. Phys.*, 2014, **16**, 24575–24591.
18 T. Mayeshiba and D. Morgan, *Phys. Chem. Chem. Phys.*, 2015, **17**, 2715–2721.
19 N. Tsvetkov, Q. Lu, Y. Chen and B. Yildiz, *ACS Nano*, 2015, **9**, 1613–1621.
20 W. Shen and J. L. Hertz, *J. Mater. Chem. A*, 2015, **3**, 2378–2386.
21 J. Hinterberg, T. Zacherle and R. A. De Souza, *Phys. Rev. Lett.*, 2013, **110**, 205901.
22 R. A. De Souza, A. Ramadan and S. Hörner, *Energy Environ. Sci.*, 2012, **5**, 5445–5453.
23 U. Aschauer, R. Pfenninger, S. M. Selbach, T. Grande and N. A. Spaldin, *Phys. Rev. B: Condens. Matter Mater. Phys.*, 2013, **88**, 54111.
24 Z. Cai, Y. Kuru, J. W. Han, Y. Chen and B. Yildiz, *J. Am. Chem. Soc.*, 2011, **133**, 17696–17704.
25 A. Kushima, S. Yip and B. Yildiz, *Phys. Rev. B: Condens. Matter Mater. Phys.*, 2010, **82**, 1–6.
26 D. Pergolesi, V. Roddatis, E. Fabbri, C. W. Schneider, T. Lippert, E. Traversa and J. A. Kilner, *Sci. Technol. Adv. Mater.*, 2015, **16**, 15001.
27 J. L. M. Rupp, S. Schweiger and F. Messerschmitt, Patent WO2014170023, 2014.
28 S. Sanna, V. Esposito, J. W. Andreasen, J. Hjelm, W. Zhang, T. Kasama, S. B. Simonsen, M. Christensen, S. Linderoth and N. Pryds, *Nat. Mater.*, 2015, **14**, 1–5.
29 L. Sun, D. Marrocchelli and B. Yildiz, *Nat. Commun.*, 2015, **6**, 6294.
30 J. L. M. Rupp, E. Fabbri, D. Marrocchelli, J.-W. Han, D. Chen, E. Traversa, H. L. Tuller and B. Yildiz, *Adv. Funct. Mater.*, 2014, **24**, 1562–1574.
31 S. Omar, E. D. Wachsman, J. L. Jones and J. C. Nino, *J. Am. Ceram. Soc.*, 2009, **92**, 2674–2681.
32 M. Mogensen, N. Sammes and G. Tompsett, *Solid State Ionics*, 2000, **129**, 63–94.
33 M. Sillassen, P. Eklund, N. Pryds, E. Johnson, U. Helmersson and J. Bøttiger, *Adv. Funct. Mater.*, 2010, **20**, 2071–2076.
34 S. R. Bishop, D. Marrocchelli, C. Chatzichristodoulou, N. H. Perry, M. B. Mogensen, H. L. Tuller and E. D. Wachsman, *Annu. Rev. Mater. Res.*, 2014, **44**, 205–239.

35 H. L. Tuller and S. R. Bishop, *Annu. Rev. Mater. Res.*, 2011, **41**, 369–398.
36 A. Evans, A. Bieberle-Hütter, J. L. M. Rupp and L. J. Gauckler, *J. Power Sources*, 2009, **194**, 119–129.
37 J. L. Hertz and H. L. Tuller, *J. Electrochem. Soc.*, 2007, **154**, B413.
38 G. Beck, H. Fischer, E. Mutoro, V. Srot, K. Petrikowski, E. Tchernychova, M. Wuttig, M. Ruhle, B. Luersen and J. Janek, *Solid State Ionics*, 2007, **178**, 327–337.
39 C. D. Baertsch, K. F. Jensen, J. L. Hertz, H. L. Tuller, S. T. Vengallatore, S. M. Spearing and M. A. Schmidt, *J. Mater. Res.*, 2004, **19**, 2604–2615.
40 C.-C. Chao, C.-M. Hsu, Y. Cui and F. B. Prinz, *ACS Nano*, 2011, **5**, 5692–5696.
41 P. Su, C. Chao, J. Shim, R. Fasching and F. Prinz, *Nano Lett.*, 2008, **8**, 2289–2292.
42 P.-C. Su and F. B. Prinz, *Microelectron. Eng.*, 2011, **88**, 2405–2407.
43 K. Song, H. Schmid, V. Srot, E. Gilardi, G. Gregori, K. Du, J. Maier and P. A. Van Aken, *APL Mater.*, 2014, **2**, 32104.
44 M. C. Göbel, G. Gregori and J. Maier, *Phys. Chem. Chem. Phys.*, 2011, **13**, 10940–10945.
45 F. Giannici, G. Gregori, C. Aliotta, A. Longo, J. Maier and A. Martorana, *Chem. Mater.*, 2014, **26**, 5994–6006.
46 B. Scherrer, S. Heiroth, R. Hafner, J. Martynczuk, A. Bieberle-Hütter, J. L. M. Rupp and L. J. Gauckler, *Adv. Funct. Mater.*, 2011, **21**, 3967–3975.
47 B. Scherrer, J. Martynczuk, H. Galinski, J. G. Grolig, S. Binder, A. Bieberle-Hütter, J. L. M. Rupp, M. Prestat and L. J. Gauckler, *Adv. Funct. Mater.*, 2012, **22**, 3509–3518.
48 M. A. Laguna-Bercero, *J. Power Sources*, 2012, **203**, 4–16.
49 I. Garbayo, A. Tarancón, J. Santiso, F. Peiró, E. Alarcón-LLadó, A. Cavallaro, I. Gràcia, C. Cané and N. Sabaté, *Solid State Ionics*, 2010, **181**, 322–331.
50 K. Kerman, S. Xuza and S. Ramanathan, *J. Electroceram.*, 2015, **34**, 91–99.
51 K. Kerman, T. Tallinen, S. Ramanathan and L. Mahadevan, *J. Power Sources*, 2013, **222**, 359–366.
52 Y. Safa, T. Hocker, M. Prestat and A. Evans, *J. Power Sources*, 2014, **250**, 332–342.
53 N. Schichtel, C. Korte, D. Hesse and J. Janek, *Phys. Chem. Chem. Phys.*, 2009, **11**, 3043–3048.
54 J. L. M. Rupp, *Solid State Ionics*, 2012, **207**, 1–13.
55 N. Yang, Y. Shi, S. Schweiger, E. Strelcov, A. Belianinov, V. Foglietti, P. Orgiani, G. Balestrino, S. V Kalinin, J. L. M. Rupp and C. Aruta, *ACS Appl. Mater. Interfaces*, 2016, **8**, 14613–14621.
56 A. Atkinson and T. M. G. M. Ramos, *Solid State Ionics*, 2000, **129**, 259–269.
57 D. Marrocchelli, S. R. Bishop, H. L. Tuller and B. Yildiz, *Adv. Funct. Mater.*, 2012, **22**, 1958–1965.
58 D. Marrocchelli, S. R. Bishop and J. Kilner, *J. Mater. Chem. A*, 2013, **1**, 7673.
59 M. Burbano, S. Nadin, D. Marrocchelli, M. Salanne and G. W. Watson, *Phys. Chem. Chem. Phys.*, 2014, **16**, 8320–8331.
60 N. Goykhman, Y. Feldman, E. Wachtel, A. Yoffe and I. Lubomirsky, *J. Electroceram.*, 2014, **33**, 180–186.
61 F. Klein and C. Müller, *Encykl. der Math. Wissenschaften, IV/4*, Teubner, 1910, pp. 311–385.
62 F. D'Heurle, *Metall. Mater. Trans. B*, 1970, **1**, 725–732.
63 D. W. Hoffman and J. A. Thornton, *Thin Solid Films*, 1977, **45**, 387–396.
64 H. Windischmann, *J. Appl. Phys.*, 1987, **62**, 1800.
65 D. J. Quinn, B. Wardle and S. M. Spearing, *J. Mater. Res.*, 2008, **23**, 609–618.
66 J. L. M. Rupp, B. Scherrer and L. Gauckler, *Phys. Chem. Chem. Phys.*, 2010, **12**, 11114–11124.
67 J. R. McBride, K. C. Hass, B. D. Poindexter and W. H. Weber, *J. Appl. Phys.*, 1994, **76**, 2435.
68 X. S. Zhao, Y. R. Ge, J. Schroeder, P. D. Persans, X. S. Zhao, Y. R. Ge, J. Schroeder and P. D. Persans, *Appl. Phys. Lett.*, 1994, **65**, 2033–2035.
69 M. Kuhn, S. R. Bishop, J. L. M. Rupp and H. L. Tuller, *Acta Mater.*, 2013, **61**, 4277–4288.
70 S. Ackermann, L. Sauvin, R. Castiglioni, J. L. M. Rupp, J. R. Scheffe and A. Steinfeld, *J. Phys. Chem. C*, 2015, **119**, 16452–16461.
71 M. J. Süess, R. A. Minamisawa, R. Geiger, K. K. Bourdelle, H. Sigg and R. Spolenak, *Nano Lett.*, 2014, **14**, 1249–1254.
72 Z. D. Dohčević-Mitrović, M. J. Šćepanović, M. U. Grujić-Brojčin, Z. V. Popović, S. B. Bošković, B. M. Matović, M. V. Zinkevich and F. Aldinger, *Solid State Commun.*, 2006, **137**, 387–390.
73 K. C. Anjaneya, G. P. Nayaka, J. Manjanna, G. Govindaraj and K. N. Ganesha, *J. Alloys Compd.*, 2013, **578**, 53–59.
74 J. Rupp and L. Gauckler, *Solid State Ionics*, 2006, **177**, 2513–2518.
75 K. Mohan Kant, V. Esposito and N. Pryds, *Appl. Phys. Lett.*, 2012, **100**, 33105.
76 D. Marrocchelli, C. Chatzichristodoulou and S. R. Bishop, *Phys. Chem. Chem. Phys.*, 2014, **16**, 9229–9232.
77 A. Kushima and B. Yildiz, *J. Mater. Chem.*, 2010, **20**, 4809–4819.
78 M. Kubicek, Z. Cai, W. Ma, B. Yildiz, H. Hutter and J. Fleig, *ACS Nano*, 2013, **7**, 3276–3286.

